Materials Science & Engineering A 838 (2022) 142770

Contents lists available at ScienceDirect

Materials Science & Engineering A

journal homepage: www.elsevier.com/locate/msea

Effects of a modified heat-treatment on microstructure and mechanical properties of additively manufactured Inconel 718

Ali Tajyar [a], Nicholas Brooks [a], Noah Holtham [a], Russell Rowe [a], David J. Newell [b], Anthony N. Palazotto [c], Keivan Davami [a,*]

[a] Department of Mechanical Engineering, University of Alabama, Tuscaloosa, AL, 35487, USA
[b] Air Force Research Laboratory, Aerospace Systems Directorate, WPAFB, OH, 45433, USA
[c] Department of Aeronautics and Astronautics, Air Force Institute of Technology, WPAFB, OH, 45433, USA

ARTICLE INFO

Keywords:
Inconel 718
Precipitation
Heat Treatment
Laser Powder Bed Fusion
Microstructural Evolution

ABSTRACT

The effectiveness of a modified heat treatment on the microstructure and mechanical properties of Inconel 718 (IN718) fabricated by the laser powder bed fusion (LPBF) technique was investigated in this work. A modified solution heat treatment (MSHT) conducted at 1160 °C for 4 h was applied to both a specimen printed in the X–Y orientation as well as another printed in the X–Z orientation. Following MSHT, the specimens were treated in two stages at 720 °C for 8 h and then again at 620 °C for 8 h. Microstructural data such as grain morphology, size, recrystallization, and texture were studied along with mechanical properties. The MSHT treatment was successful in removing the Laves phase, cellular-dendritic structure, and segregations but the metal carbides (MC-type carbides) remained around grain boundaries. Additionally, recrystallization and grain growth led to an equiaxed microstructure for both specimen orientations. Precipitated γ′ and γ″ phases were revealed within the microstructure via transmission electron microscopy (TEM) following the two-stage aging process. Micro and nanoindentation measurements were performed to validate mechanical property evolution. Hardness values decreased following the MSHT treatment but greatly improved following the aging procedure which is attributed to the dissolution of microstructural inhomogeneities during MSHT and subsequent precipitation of uniformly distributed fine γ′ and γ″ particles following the aging stages. The microstructure and mechanical properties of additively manufactured IN718 can be significantly improved through use of proper solutionizing and aging heat-treatments.

1. Introduction

IN718 is one of the most widely used nickel-based superalloys for extreme environment applications related to aerospace, energy, and marine industries. Its superior mechanical strength at temperatures up to 650 °C along with its excellent corrosion and creep resistance have proven extremely beneficial in high-temperature environments [1]. The superior high-temperature mechanical properties of IN718 are a direct result of precipitated γ′ (Ni_3(Al,Ti)) and γ″ (Ni_3Nb) intermetallic phases within the γ matrix which inhibit the motion of dislocations. During precipitation of these hardening phases other intermetallic phases such as the orthorhombic δ phase, carbides (MC, $M_{23}C6$, M_6C), and the hexagonal Laves phases $(Ni,Cr,Fe)_2(Nb,Mo,Ti)$ may also be formed [2,3].

Additive manufacturing (AM) has become an increasingly popular technique for producing nickel-based superalloy components due to its advantages over traditional subtractive methods, including superior design flexibility and reduced material waste [4,5]. Powder bed fusion technologies like LPBF have been widely recognized as a promising AM technology for manufacturing IN718 parts [6,7]. Despite the promising advantages of LPBF, a comprehensive study focused on optimizing the microstructural properties of the material during fabrication must be pursued in order to mitigate defects and produce high performance products [6,8]. Columnar grains with a vertical crystal orientation are attributed to the rapid solidification and high thermal gradients that occur during fabrication of the component using LPBF. This results in an undesirable anisotropy of mechanical behavior throughout the component, especially when fabricating components with complex geometries [9–11].

To mitigate the defects introduced during fabrication of the AM

* Corresponding author.
E-mail address: kdavami@eng.ua.edu (K. Davami).

https://doi.org/10.1016/j.msea.2022.142770
Received 20 September 2021; Received in revised form 30 January 2022; Accepted 31 January 2022
Available online 3 February 2022

IN718, post-processing heat treatments are often used to try to produce a more isotropic material with fewer microstructural defects [12]. The addition of post processing heat treatments might lead to the formation of carbides, Laves, δ, γ′, and γ″ phases in AM IN718 which have a significant effect on the mechanical properties of the material [6,13,14]. Zhou et al. investigated the microstructural and mechanical properties of various heat treated LPBF IN718 specimens. It was observed that the solution heat treatment at 980 °C was not capable of dissolving the Laves phases and instead resulted in the formation of the δ-phase. At 1065 °C, solution heat treatment completely removed the segregation. Additionally, the amount and distribution of γ′ and γ″ precipitates were investigated after two-stage aging of alloys [15]. The microstructure, mechanical properties, and phase formations were characterized for traditional homogenization, double-aging heat treatment, and a modified heat treatment, which included higher temperature homogenization with a one-time lower temperature aging treatment of AM IN718 by Li et al. [16]. Their observation was that the modified heat treatment maintained the ultimate strength achieved by the traditional heat treatment while also increasing the plasticity. The increased plasticity was due to the recrystallized grains with annealing twins, while the strength was maintained due to the fine γ′ and γ″ precipitates.

The purpose of this study is to better understand how post-processing heat treatments affect the microstructure and mechanical properties of LPBF fabricated IN718 samples. For this research, as-built LPBF IN718 specimens were subjected to a MSHT followed by a two-stage aging heat treatment (AHT). The specimens were fabricated in the transverse (X–Y plane) and parallel (X–Z plane) build directions. MSHT took place at 1160 °C for a duration of 4 h and was then followed by a two-stage AHT. Optical microscopy, scanning electron microscopy (SEM), and transmission electron microscopy (TEM) were used to analyze the microstructure in the as-built and heat-treated specimens, while nano and microindentation tests were performed to evaluate the mechanical properties.

2. Experimental procedures

2.1. Material

Powder Alloy Corporation (Loveland, Ohio, USA) provided the IN718 powder. The elemental compositions of the powder are shown in Supplementary Information (Table S1). The alloy was powderized into spherical particles with diameters between 25 μm and 40 μm using gas atomization. An *M2 cusing* Concept Laser (Lichtenfels, Germany) printer equipped with a 400 W continuous-wave ytterbium fiber laser was used to fabricate specimens. Argon gas was used to minimize oxidation during specimen fabrication. The two different fabrication orientations of the specimens in the X–Y and X–Z plane are shown in Supplementary Information (Fig. S1).

2.2. Post-process heat treatments

The post processing heat treatment stages are shown in Table 1. The modified solution heat treatment (MSHT) heats the specimen to 1160 °C for 4 h. The MSHT is above the solvus temperature of the precipitates and therefore secondary phases (δ, γ', and γ") as well as Laves phases should completely dissolve into the γ matrix. To prevent precipitation during the cooling process, the specimens were water quenched immediately after annealing. The MSHTed specimens were then treated with a two-step aging heat treatment consisting of two thermal exposures at 720 °C for 8 h, furnace cooling to 620 °C for 8 h, and a final air-cooling stage (AHT specimens). MSHT and AHT specimens were then compared with the baseline as-built specimens from each orientation (AB specimens).

Table 1
List of heat treatment conditions.

Designation	Heat treatment condition
AB	As-built condition with no post-treatment
MSHT	MSHT at 1160 °C for 4 h + WQ
AHT	MSHT at 1160 °C for 4 h + WQ + double aged at 720 °C for 8 h (furnace cooled to 620 °C), then held at 620 °C for 8 h (followed by air cooling)

Note: "WQ" refer to water quenching.

2.3. Microstructural characterization methods

The three specimens (AB, MSHT, AHT) were mounted in conductive resin, ground from 240 to 4000 grit, and then polished using diamonds suspension of 3 μm, 1 μm, and 0.05 μm colloidal silica suspension to achieve a good surface finish for microstructural analysis. After polishing, the specimens were then etched using Kalling's No. 2 etchant for a few seconds. Optical microscopy was conducted using a Zeiss Axio Scope A1 microscope. Scanning electron microscopy (SEM, Thermo Scientific™ Apreo) along with energy dispersive spectroscopy (EDS) and electron backscatter diffraction (EBSD) were used to microstructurally and crystallographically characterize the specimens before and after heat treatment. EBSD was conducted using a 10 kV voltage, at a working distance of 16 mm using a 0.3 μm step size. Grain size and shape as well as Kernel averaged misorientation (KAM) maps were extracted from the EBSD and SEM images. EDS was performed to determine elemental composition of precipitates and observe element segregation. Transmission electron microscopy (TEM, FEI *Tecnai F-20*) foils approximately 10 μm in length and 5 μm in width were extracted from the surfaces of the pre and post heat treatment X–Y specimens through focused ion beam (FIB) milling. Dislocation density, microstructural evolution due to heat treatment, and precipitate morphology were obtained from TEM imaging.

2.4. Mechanical testing

Room-temperature nanoindentation and microindentation tests were performed on the as-built and the heat-treated specimens. Nanoindentation tests were performed using an Anton-Paar TTX-NHT^3 nanoindentation tester equipped with a diamond pyramid Berkovich indenter tip. Measurements including the elastic modulus (*EIT*) and nanohardness (*HIT*) were obtained using nanoindentation. A force of 200 mN, a dwell time of 5 s, and Poisson's ratio of 0.29 were chosen as input parameters for IN718 nanoindentation tests. 27 indents were performed on each specimen with a 200 μm separation to avoid any interference between indents. Additionally, microhardness tests were performed with a Vickers microhardness tester (Clemex Technologies Inc., Canada). A 3 × 3 indent matrix with a separation of 300 μm, a force of 300 gf (~3 N), and a dwell time of 10 s was performed on each specimen.

3. Results

3.1. Microstructure analysis

3.1.1. As-built IN718 alloy

Optical microscopy micrographs for the X–Y and X–Z planes of the as-built specimens are shown in Fig. 1. In both orientations, the microstructure is uniform and has desirable metallurgical bonding between adjacent layers and tracks. This indicates that sufficient thermal energy was applied by the laser to fully melt the IN718 powder (melting temperature of 1340–1364 °C [17]) and the previously solidified layers [18]. The X–Y specimen shows a columnar pattern whereas the X–Z specimen exhibits a "fish scale" pattern which are both characteristic of the LPBF AM process [14,15]. The direction of the columnar pattern in the X–Y orientation corresponds to the scan rotation between adjacent layers during printing (Fig. 1(a)) [15]. The patterns shown in Fig. 1(b) is

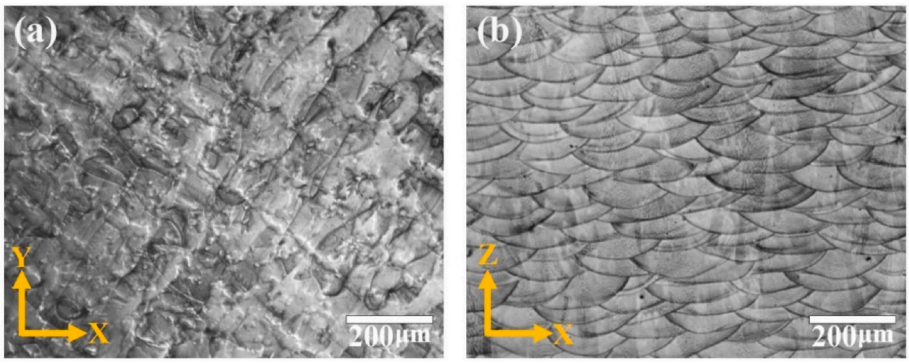

Fig. 1. Optical micrographs of the as-built IN718 alloy from the (a) X–Y and (b) X–Z specimens.

a result of the Gaussian energy distribution in the X–Z plane of the laser [19].

Analysis of the grain morphology and crystallographic orientation was conducted using Electron Back Scatter Diffraction (EBSD) in a scanning electron microscope (SEM, Thermo Scientific™ Apreo) shown in Fig. 2. In the as-built X–Y specimen, fine and coarse grain zones are distributed throughout the build plane and the shape of the grains is irregular equiaxed. The grains along the X–Z plane (Fig. 2(d)) show a strong columnar texture along the <001> direction (red grains) and a less prominent texture in the <101> direction (green grains). The cumulative probability plot of grain size distribution is shown in Fig. 3. An average grain size of 27.2 μm and 45.8 μm was recorded for the X–Y and X–Z specimens, respectively.

By comparing the size of the columnar grain size in Fig. 2(d) and the "fish scale" melt pools in Fig. 1(b), it can be seen that some grains cross over melt pool boundaries. This microstructure is a result of epitaxial, dendritic grain growth determined by the directional heat flux during LBPF of FCC structure, which crystallographically favors the <001> orientation [20,21]. Heat primarily dissipates downwards through the substrate or pre-deposited layers during the LPBF process. Therefore, the heat flow during the solidification process is directed roughly perpendicular to the substrate or pre-deposited layers which results in preferential orientation columnar grains [21,22]. Some fine grains, orientated mostly in the <111> direction, are dispersed throughout the columnar as-built microstructure with a density much less than the grains oriented with <100> parallel to the build direction [2,23]. Due to layer or track overlapping during the LPBF process, the overlapped material is re-melted and re-solidifies, meanwhile the surrounding coarse grains are melted and recrystallized. This explains the presence of fine grains around the coarse grains in the as-built sample [22,24].

SEM micrographs of the as-built IN718 microstructure are shown in Fig. 4. A few micro-pores are evident in both orientations (Figs. 4(a) and

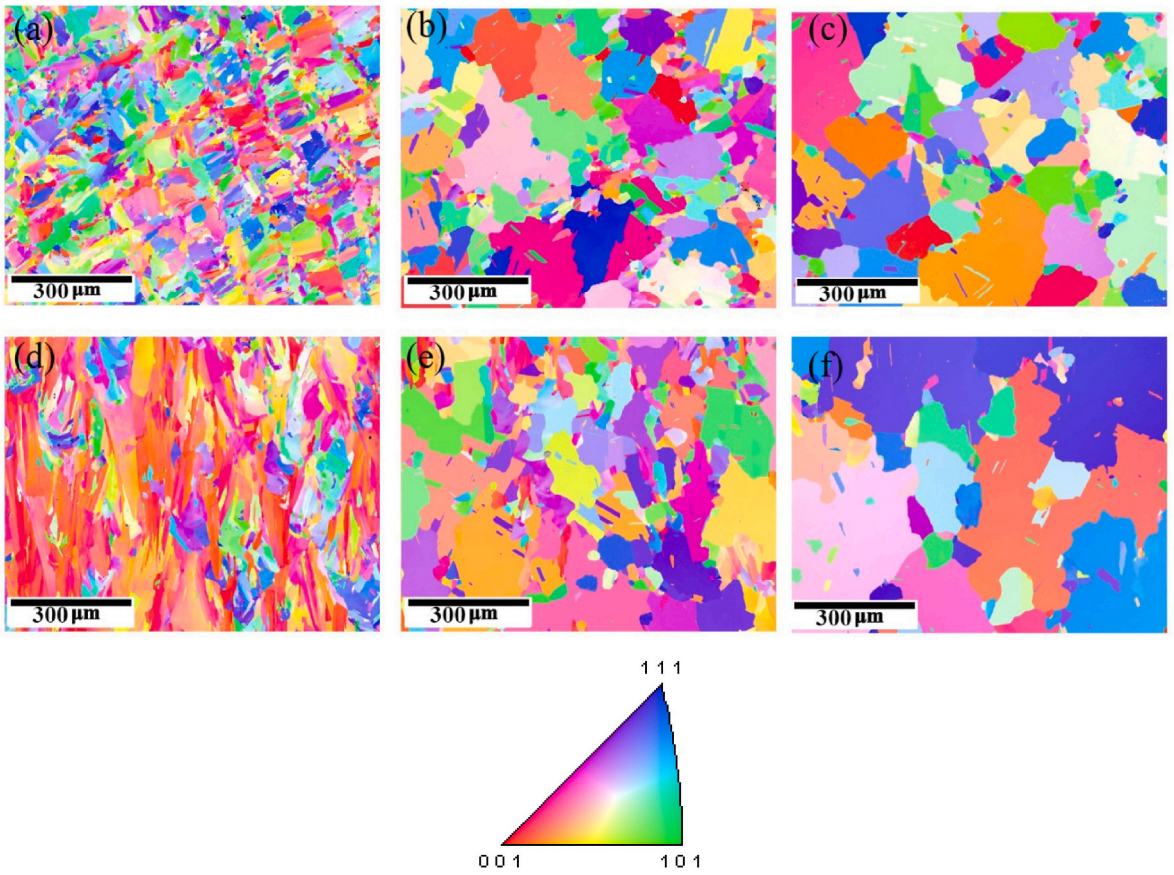

Fig. 2. IPF maps of X–Y orientation specimens: (a) the as-built, (b) MSHT, (c) AHT and X–Z orientation specimens: (d) the as-built, (e) MSHT, (f) AHT.

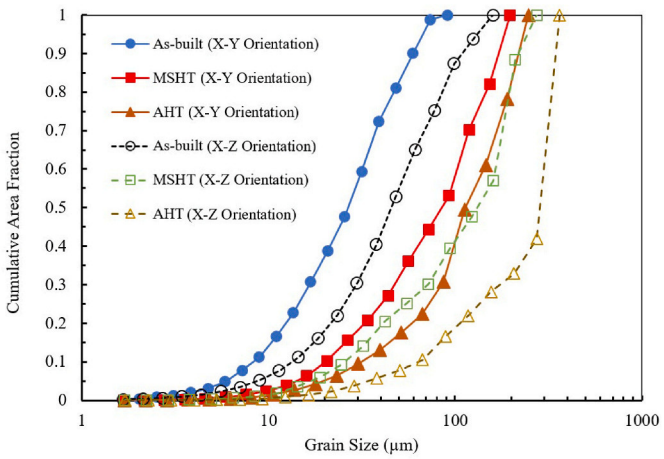

Fig. 3. Cumulative area fractions for the grain size distribution related to before and after post heat treatments of MSHT (Modified solution heat treatment) and AHT (MSHT + Double aging).

4(b)). During the LPBF process, the rapid molten dynamics of the melted metal cause gas bubbles to be trapped leading to micro-pore formation. No notable size difference was observed in the pores, which were less than 20 μm, between sample orientations. These pores can act as stress concentration zones which can be deleterious to the fatigue properties by causing surface discontinuities or acting as sites for fatigue initiation [25–27]. Optimizing fabrication parameters such as layer thickness, laser power, scan speed, and including post-processing heat treatments can effectively minimize component porosity [25,28].

A non-uniform, dense, cellular, and columnar dendritic microstructure, several tens of microns in length, is shown in Figs. 4(c) and 4(d) for the X–Y and X–Z orientations, respectively. In the X–Y orientation, Fig. 4 (c), the columnar dendrites are observed to grow in multiple directions within a single melt pool. However, due to preferential cooling during scanning, the direction of dendrite growth in the X–Z orientation, Fig. 4 (d), is mostly parallel to the direction of deposition. Micro-segregation of heavier elements to the interdendritic region creates a sharp contrast between the darker dendritic core in Figs. 4(c) and 4(d). Rapid solidification during the LPBF entirely prevents macro-segregation, however, it does not prevent micro-segregation [6], as seen in Figs. 4(c) and 4(d).

The details of columnar/cellular microstructure of the LPBF IN718 specimens are shown in Figs. 4(e) and 4(f). Columnar/cellular substructures are contained within each grain for both specimens. The cross-sectional size of most cells or dendrites is less than 2 μm. High resolution SEM micrographs of a grain in the X–Y specimen are shown in Fig. 5(a). White discontinuous stripes inside grains and along grain boundaries indicate that solidification segregation occurs not only along grain boundaries, but also inside the grains. The TEM bright field image in Fig. 5(b) displays a magnified view within a grain. As can be seen, fine

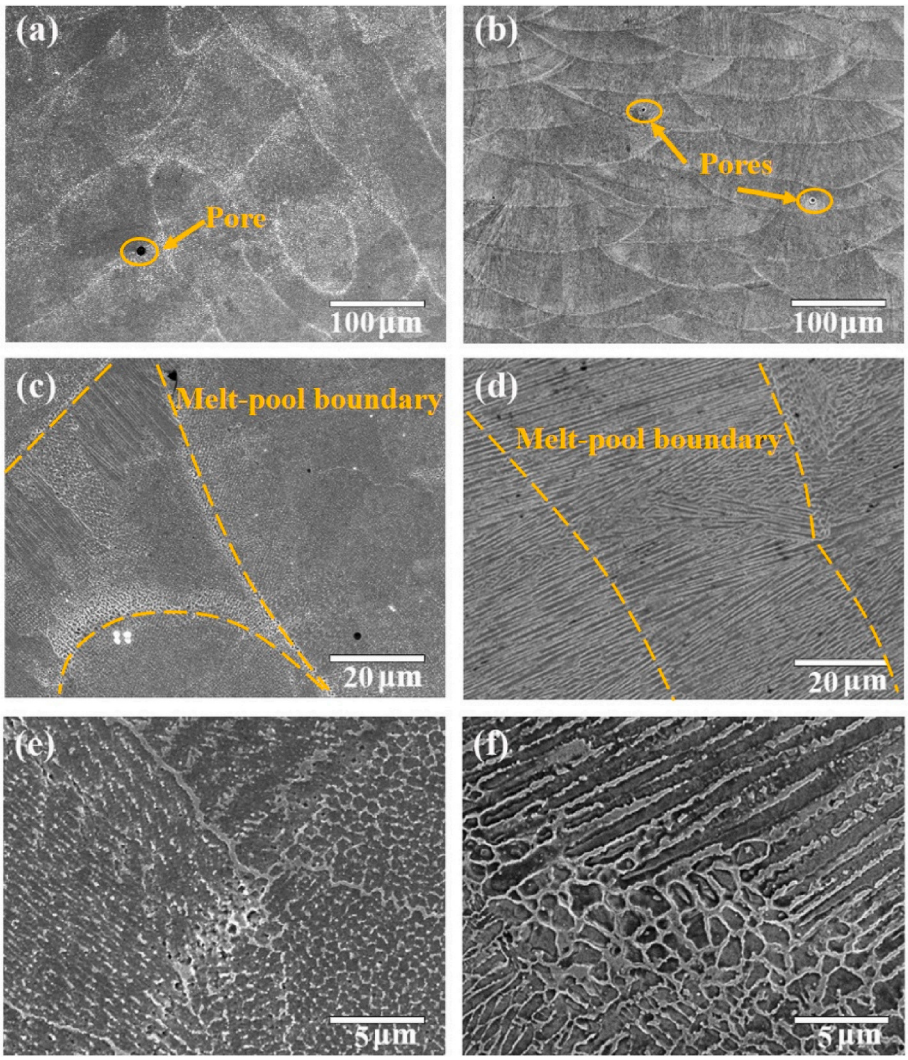

Fig. 4. SEM micrographs from the as-built IN718 specimens: (a, c, e) X–Y and (b, d, f) X–Z orientations.

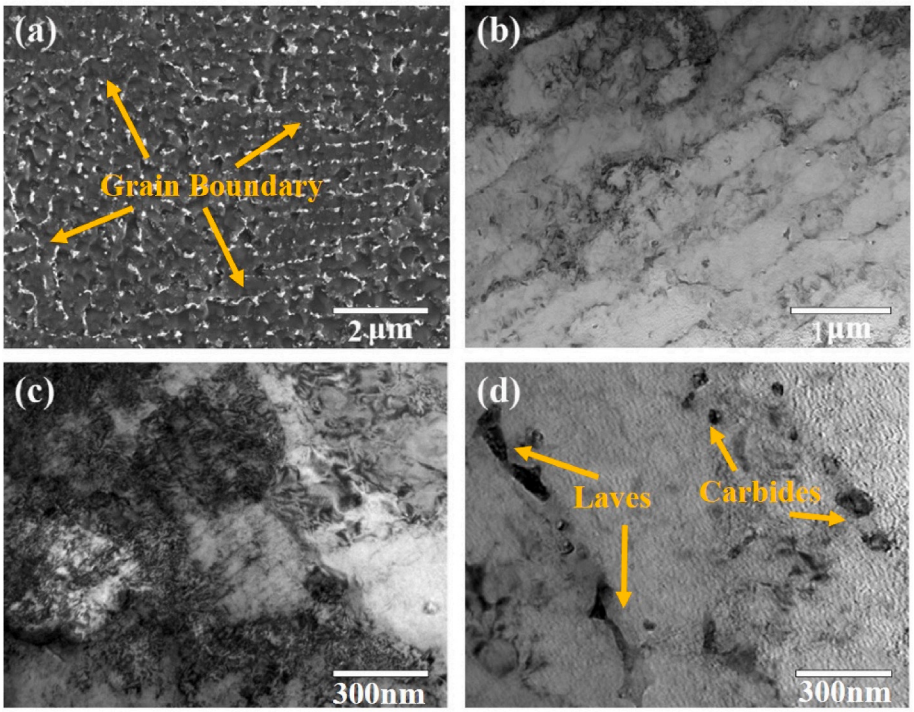

Fig. 5. (a) High magnification SEM micrographs from the as-built X–Y specimen, (b) TEM bright field image showing cellular subgrain microstructure, (c) TEM bright field image showing high dislocation density microstructure, and (d) TEM bright field image showing Laves phases and carbide particles in the as-built IN718 specimen (X–Y orientation).

cellular sub-structures (sub-grain structure) exist in the microstructure of as-built IN718 specimen. Multiple colors shown within a single grain, Figs. 2(a) and 2(d) could be a result of sub-grains, as each sub-grain can have a slightly different crystallographic orientation [29]. As shown in Fig. 5(c), the high density of dislocation structure was preferentially located at the cellular boundary, indicative of residual stress in IN718 specimen fabricated by LPBF. It was reported that this dislocation sub-grain structure can positively affect both the ductility and strength simultaneously. Moreover, as depicted in Fig. 5(d), the irregular block-shaped precipitates, mostly located at the substructure's boundaries, and globular particles are visible and can be identified as Laves phases and carbide particles, respectively. Aside from Laves phases and carbides, almost no other precipitates such as δ, γ′ and γ″ phases can be observed. The complex physical metallurgy in the molten pool caused by the high-energy laser beam during the LPBF process and the rapid cooling rate (105–107 K/s) during the solidification may result in numerous sub-grain structures inhibiting the precipitation of these phases (δ, γ′ and γ″) [22,28].

Energy dispersive spectroscopy (EDS) was conducted on the white regions observed in Figs. 4 and 5 and the compositional results are shown in Fig. 6 (Additional information in SI). The varying thermal histories which are inherent to the AM process can lead to significant differences in the phase composition and microstructure of LPBF IN718 components. Elements such as Nb, Mo, Ti and C are highly susceptible to segregation in the IN718 alloy and the distribution of Nb is particularly important with regard to its lowest value of partition coefficient (<0.5) [6]. The EDS maps in Fig. 6 shows that Ni, Fe, and Cr, which comprise the primary γ phase, are uniformly distributed (dark gray regions) whereas micro-segregation of Nb, Mo, Ti, and C can be seen in the white regions. This micro-segregation of these elements can result in the formation of the Laves phase $(Ni,Cr,Fe)_2(Nb,Mo,Ti)$ and carbides particles (Ti, Nb)C (globular particle in Fig. (6)) in the as-built IN718 specimen.

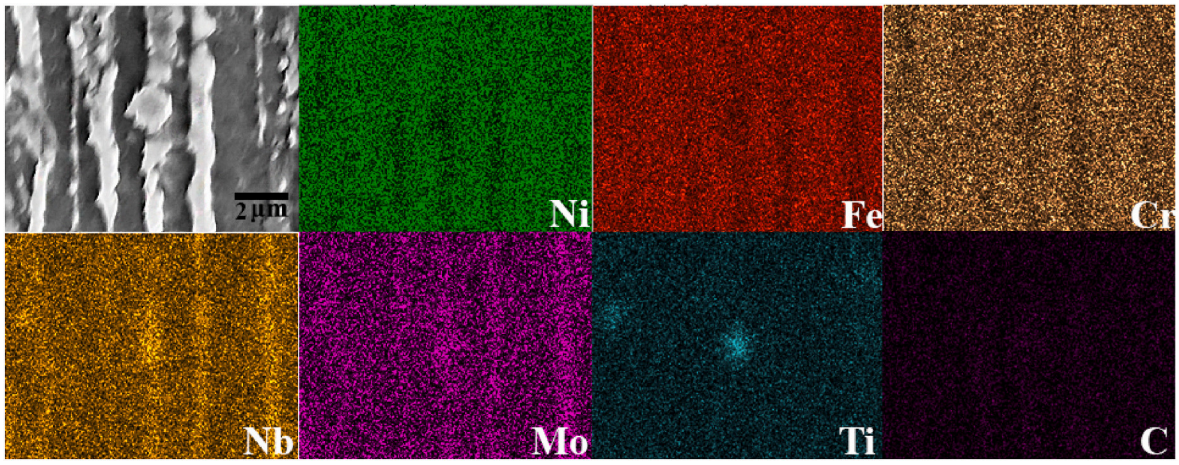

Fig. 6. EDS analysis of the white interdendritic region from as-built specimens (X–Z orientation).

3.1.2. MSHT IN718 alloy

The EBSD maps in Figs. 2(b) and 2(e) show that after the MSHT, the grains in both specimens are more equiaxed in nature and presented a more random texture than the as-built material. Additionally, the columnar/cellular structures in the as-built material recrystallized and a homogenized microstructure is observed. It should be noted that annealing twins, which could lead to decreased fatigue performance [21], were present after MSHT. Grain morphology in each specimen following the MSHT is pictured in Fig. 7. Elemental segregation and melt pool patterns disappeared and grains grew up to 274 μm in size after exposure to 1160 °C for 4 h (Fig. 3). The selected temperature is above the solvus temperature of the δ phase in Inconel 718. The solvus temperature lays between 1005 and 1015 °C for Nb contents of 5.06 and 5.41 wt%, respectively. Also, at this temperature, the Laves phase becomes dissolved completely. Grain boundary migration driven by the diffusion of atoms with a high segregation rate, such as Nb, is the likely mechanism behind grain growth. This is known as diffusion induced grain boundary migration [21] and has been shown in both theoretical and experimental [30,31] works to be driven by one or more combinations of energy sources such as coherency strain energy, capillary energy, chemical energy, and stored energy. IN718 contains several elements and a number of secondary phases which all contribute to driving the diffusion induced grain boundary migration effect [29].

White particles along the grain boundaries in Fig. 7 were examined by EDS (Fig. 8) and found to be rich in Ti, Nb, Mo, and C which indicates that the particles are likely carbides that have survived the MSHT process rather than Laves phases. It is evident that exposure at 1160 °C was sufficient for the dissolution of Laves phases as well as the coarsening of carbides. Carbides are very stable at high temperatures with a melting point of 3600 °C for NbC [32] as compared to 1364 °C for IN718 [33]. The high temperature of MSHT, while not enough to melt carbides, is enough to increase the diffusion rate and promote carbide coarsening [17], as well as the segregation of carbide-forming elements such as C and Nb which encourages carbide precipitation [19,34]. Carbides similar to those seen in this work were also observed in Refs. [6,29] where LPBF IN718 was solutionized at 1100 °C and 1250 °C for both 1 h and 7 h. Grain-boundary carbides such as these have been shown to increase stress rupture life by pinning grain boundaries and preventing migration [12,25]. Achieving near-homogeneous microstructures in the X–Y and X–Z orientations that were not produced in the previous studies with lower solution temperatures and time is an outstanding outcome of this research [6,13,14,35].

3.1.3. AHT IN718 alloy

As shown in Figs. 2(c) and 2(f), no discernible change in grain shape is observed due to the aging heat treatment process, however the average grain size does increase (Fig. 3). The AHT specimens were examined using SEM in both the X–Y and X–Z orientations, Figs. 9(a) and 9(b), respectively. Carbides are observed along grain boundaries as well as within the grains. Further investigation using TEM (Fig. 10) identifies nanoscale γ' and γ" strengthening phases formed in the γ matrix during the aging heat treatment. The γ' precipitates, $Ni_3(Al,Ti)$, are identifiable by their spherical morphology compared to the disc shaped morphology of the γ" precipitates (Ni_3Nb) [36,37]. The γ' precipitates have an average diameter of approximately 13 nm whereas the γ" precipitates are more varied with a length between 7-35 nm and thickness of approximately 5 nm. Analysis of γ" precipitate length distribution in Fig. 10(c) shows that the mean length is 14 nm. A comparison of the sizes for the γ' and γ" precipitates formed during different heat treatments is shown in Table 2. Slightly finer precipitates were formed during the AHT process compared to the conventional processes. However, this slight difference in average length might be due to different calculating methods in different works. Ultrafine γ" typically have good coherency strengthening effects since the γ" precipitates lose coherency with the γ-matrix when precipitates are greater than 35–40 nm [38]. The uniform distribution of γ' and γ" strengthening phases seen in the double aging heat treatment resulted from the homogenized microstructure and uniform distribution of Nb and Ti elements following the MSHT at 1160 °C/4 h. This proves that the temperature and holding time of the MSHT was sufficient to dissolve the Laves phases, allowing Nb and Ti to diffuse uniformly and completely into the γ matrix which allows the uniform and coherent precipitation of the γ'/γ" strengthening phases during the AHT [25,39].

3.1.4. Kernel averaged misorientation map

Further microstructural characterization was conducted using Kernel averaged misorientation (KAM) maps which were taken on both samples to evaluate the residual stress state and dislocation density (Fig. 11). KAM maps qualitatively display microscopic plastic strains indicated by a change in color between pixels and is closely associated with dislocation density [22]. The as-built specimens contain a large degree of plastic strain (dislocations) (Figs. 11(a) and 11(d)). High KAM values are largely located in areas containing sub-grains as well as near grain boundaries containing Laves phases (high-Nb content). Average KAM values for the as-built X–Z and X–Y oriented specimens are 0.59 and 0.61, respectively. The repeated rapid heating and cooling cycles inherent to the LPBF process create plastic strain and thus residual stresses in the structure. These two induce the formation of dislocation networks. Therefore, it can be concluded that areas with larger KAM values in the as-built specimen contain a high dislocation density which can be attributed to the plastic deformation and associated residual stresses that the material experiences during the melt-solidification process [14,16,29]. These results agree well with TEM findings which also show a high dislocation density in the as-built specimens (Fig. 5(c)).

In contrast, KAM maps taken of the MSHT specimens show a clear decrease in dislocation density. Average KAM values for the X–Y and X–Z oriented specimens were 0.41 and 0.39, respectively, which can be attributed to MSHT reliving the internal strains within the as-built

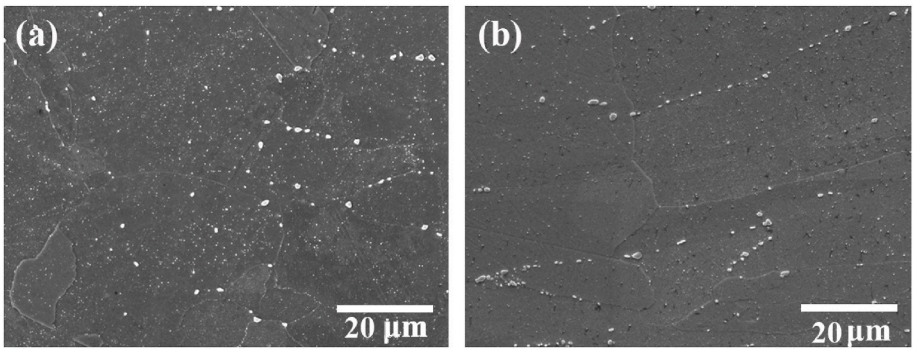

Fig. 7. SEM images of MSHT specimens in the (a) X–Y and (b) X–Z cross-sections. Visual examination of the images demonstrates segregated particles along/adjacent grain boundaries and particles in the grain interior. These particles are identified as carbides.

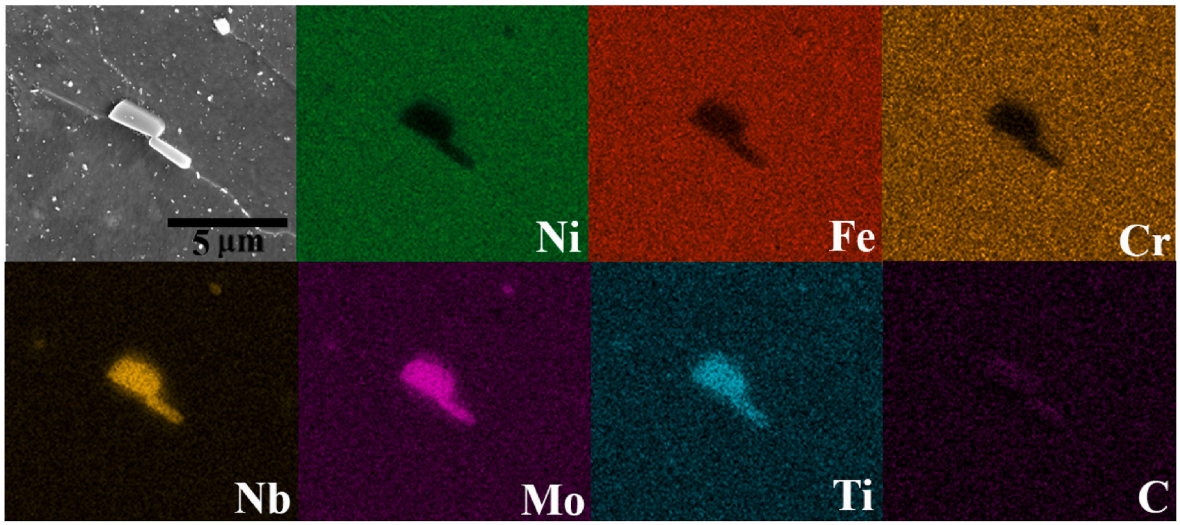

Fig. 8. EDS analysis on the particles along grain boundaries and in the grain interior.

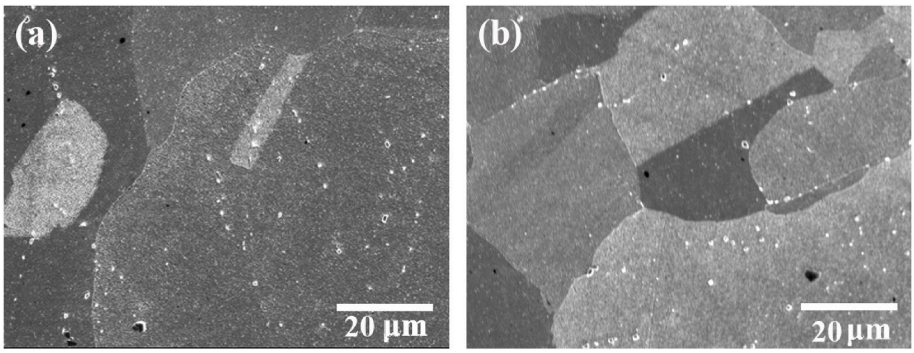

Fig. 9. SEM images of AHT specimens in the (a) X–Y and (b) X–Z orientations.

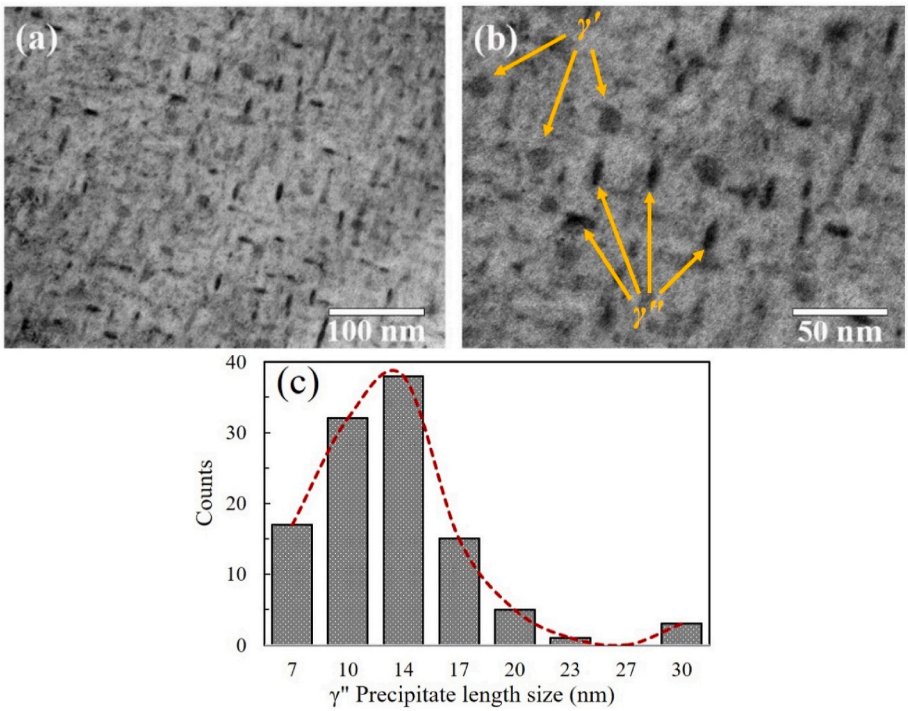

Fig. 10. TEM images of AHT specimen in the X–Y orientation (a) Low magnification, (b) High magnification and (c) γ″ precipitate length size distribution.

Table 2
Sizes of γ' and γ'' formed during conventional Direct Aging and Solution + Double Aging.

Homogenization and Solution	Aging	Size of γ'' (Length)	Size of γ' (Diameter)	
None	720 °C/8 h + 620 °C/8 h	More than 40 nm	–	[40]
980 °C/1 h	760 °C/10 h + 650 °C/8 h	60–140 nm	40 nm	[35]
980 °C/1 h	720 °C/8 h + 620 °C/8 h	30 nm	–	[40]
1065 °C/1.5 h	760 °C/10 h + 650 °C/10 h	100–400 nm	–	[16]
1065 °C/1.5 h	760 °C/10 h + 650 °C/8 h	100–200 nm	50 nm	[35]
1065 °C/1 h	720 °C/8 h + 620 °C/8 h	17 nm (average)	19 nm	[15]
1100 °C/1.5 h + 980 °C/1 h	720 °C/8 h + 620 °C/8 h	30 nm	–	[40]

material (Figs. 11(b) and 11(e)). In fact, solutionized material exposed to 1160 °C has sufficient energy to begin the process of grain growth associated with releasing the stored strain energy through dislocation annihilation [41]. Therefore, the 4 h MSHT treatment was sufficient to develop a nearly strain-free microstructure and relieve a large fraction of residual stress imparted by the AM process. Figs. 11(c) and 11(f) show little change is seen in KAM values taken before and after the aging process.

3.2. Nanomechanical properties

Nanoindentation tests were performed using an Anton-Paar TTX-NHT^3 nanoindenter to evaluate the nanomechanical properties of the as-built and heat-treated specimens in both the (X–Y) and (X–Z) orientations. The results depicted in Fig. 12 show the hardness and elastic modulus of the specimens in both the X–Y and X–Z orientations. In Fig. 12(a), it can be observed that the hardness values of X–Y and X–Z specimens are 3.18 and 3.32 GPa, respectively. Differences in the X–Y and X–Z orientations is likely attributed to the differences in grain geometry and texture and is consistent with previous research [2,15,42]. The hardness of as-built specimens can be affected by the amount and distribution of the precipitates such as the Laves phase, micro-segregation of alloying elements, and the fine cellular and columnar dendritic microstructure which can increase the hardness of the material [25,42]. The existence of phases such as Laves, limits the precipitation of strengthening phases such as γ" by consuming the available Nb. The hardness of the X–Y and X–Z specimens after MSHT are 2.79 and 2.88 GPa, respectively. Decreases in hardness values of 12–13% after MSHT could be attributed to the elevated temperature of 1160 °C where the Laves phases can completely dissolve and an equi-axed microstructure can be obtained through recrystallization. Additionally, strain in the microstructure can also lead to increased hardness values. As depicted in Fig. 11, strain can be significantly lowered using a post process stress relief step, such as MSHT. At elevated temperatures, the rate of atomic diffusion increases and allows atoms to move from high to low stress regions. This causes the grains to coarsen and the internal strain energy to be released. The grain size and hardness in metals are known to have an inverse relationship. A greater amount of strain is associated with smaller grains such that when smaller grains impede the propagation of dislocations within the material, the material experiences greater strengthening than experienced when larger grains impede the propagation of dislocations [29].

Since the MSHT is conducted at temperatures above the solvus temperature of the δ phase, a reduction in the hardness can also be attributed to its absence [43]. While the role of this phase is still being studied, previous research indicates its formation during the conventional solutionizing process [14,44] as well as the main role it plays in the mechanical properties of IN718. Its precipitation leads to grain boundary pinning. Also, within the grain, this phase contributes to the hardness by obstructing the movement of dislocations. It should be noted that as the volume fraction of the δ phase increases, Nb atoms are rapidly consumed, and this phenomena can negatively affect the desirable mechanical properties of IN718 since it leads to a decrease in the volume fraction of the γ'' phase [45–48]. Therefore, the formation of this phase needs to be precisely controlled.

After AHT, the hardness for both X–Y and X–Z specimens increases significantly to 6.14 and 6.02 GPa respectively, which is likely due to the formation of γ'' and γ' precipitates. The different lattice parameters of the γ'' and γ' phases results in a stress field that restricts dislocation movement. Precipitation hardening effects might to some extent make up for the loss [49] in strength caused by the coarse recrystallized grains

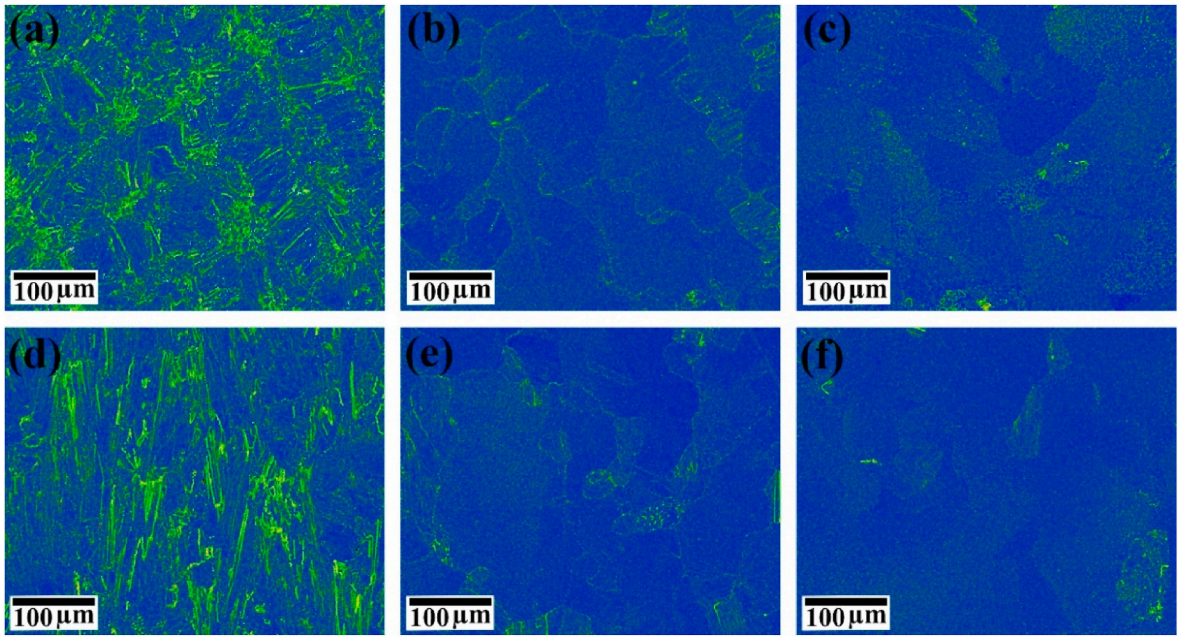

Fig. 11. KAM maps of X–Y orientation specimens: (a) the as-built, (b) MSHT, (c) AHT and X–Z orientation specimens: (d) the as-built, (e) MSHT, (f) AHT.

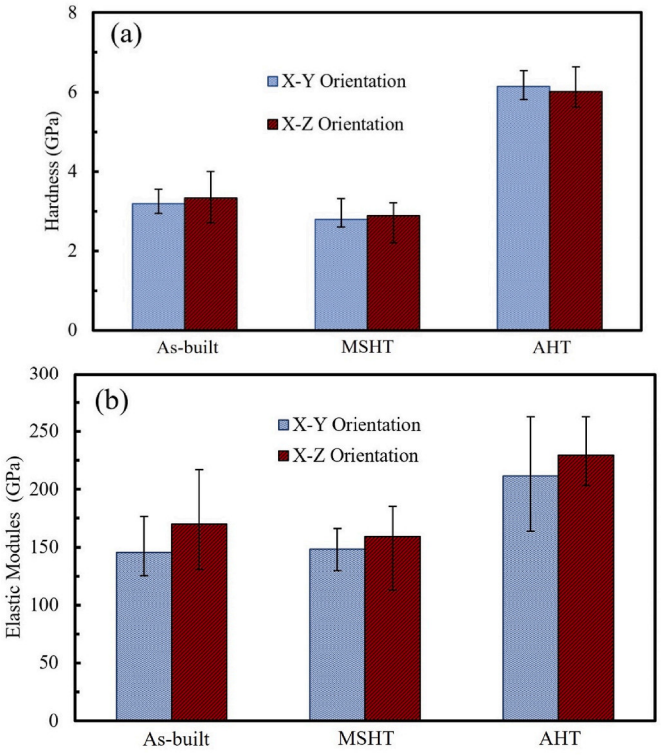

Fig. 12. Variation of (a) nanohardness and (b) Elastic modulus of as-built, MSHT and AHT specimens for X–Y and X–Z orientations.

in the AHT specimen. These ultrafine γ′ and γ″ phases greatly enhance the hardness of LPBF IN718 when they are uniformly dispersed in the matrix, making this an ideal prospect for use in high-temperature applications [35].

The average values for hardness from microindentation measurements are listed in Table 3. The as-built specimen presented microhardness values of 284 HV in the X–Y orientation and 299 HV in the X–Z orientation, while the MSHT specimens experienced a decrease in microhardness, similar to the nanohardness, of 206 HV in the X–Y orientation and 216 HV in the X–Z orientation. These results agree with previous research [2,29,42] on the microhardness of LPBF IN718. Microhardness values of the AHT specimen presented a significant increase compared to the as-built and MSHT specimens in both the X–Y and X–Z orientation of 483 HV and 489 HV, respectively. The large increase in hardness that resulted in the AHT specimen is likely attributed to the fine γ" precipitates with an average length of 14 nm that can be seen in Fig. 10(c). These fine, uniformly distributed γ' and γ" precipitates that resulted from the extra aging processes following MSHT exhibit greater coherency strength as opposed to precipitates with a diameter greater than 35–40 nm [38].

The elastic modulus values obtained from the nanoindentation technique are depicted in Fig. 12(b) for the as-built and heat-treated specimens. The average values of elastic modulus for the as-built specimens in the X–Y and X–Z specimens were 146 GPa and 170 GPa, while for the MSHT specimens in the X–Y and X–Z specimens they were 148.5 GPa and 159 GPa, respectively. These values are in agreement with what has been reported previously for AM IN718. Even though the alteration among the Young's modulus of the samples was considerable, no relation was found with the processing parameters including annealing time, scan strategy, or orientation [2,9,15,40]. The AHT specimens presented the highest elastic modulus compared to the as-built and MSHT specimens at 211 GPa in the X–Y orientation and 230 GPa in the X–Z orientation, indicating that the AHT treatment enhances the mechanical properties of the LPBF IN718 due to the formation of γ" and γ' precipitates [2,15]. The Young's modulus of the aged specimens was previously measured at the macroscale level and values in the range of 209–213 GPa were recorded [9]. While small differences between the Young's modulus obtained from the nanoindentation technique and macroscale tensile tests are expected, the results here agree well.

Table 3
Variation of microhardness of as-built, MSHT and AHT specimens for X–Y and X–Z orientations.

Heat treatment Orientation	Mean values of micro hardness (HV)		
	None	MSHT	AHT
X–Y	284	206	483
X–Z	299	216	489

4. Discussion

Due to the significant differences that exists between the microstructure of additively and traditionally manufactured Inconel 718 that are attributed to the rapid solidification process and the existing thermal gradients in the AM parts, commonly used heat treatment processes that have been developed for TM materials are not applicable, or at least are not the best choice for AM materials. The majority of the currently adopted heat treatment processes for TM specimens are conducted at temperatures less than <1100 °C which are simply not high enough to completely dissolve undesirable Laves as well as microsegregated phases that are formed during the fabrication process in the AM parts. The aforementioned results indicate that the MSHT process has the potential to achieve a homogenous microstructure with dissolved segregated precipitates, even though the carbides still remain in the matrix. In particular, the MSHT dissolved the brittle intermetallic Laves phases that are known to degrade the mechanical properties of IN718. It should be noted that this heat treatment process relaxes the residual stresses and also coarsens the grains that both affect the mechanical properties of the part after the solutionizing process.

The microscopy results clearly show the fine cellular and columnar structure of the as-built IN718. The formation of the columnar microstructure is attributed to the thermal gradient during the additive manufacturing process. The high cooling rate also encourages the formation of the dendritic microstructure [50,51]. The EBSD imaging showed that grains are elongated parallel to the print direction and the dominant orientation of the grains was along <001> direction. The microscopy results also illustrated that the MSHT above the solvus temperature of δ-phase and Laves phases that was conducted at 1160 °C for 4 h resulted in a more uniform microstructure, even though this treatment resulted in a slightly bigger carbide particles. This increase in carbide size was previously attributed to an increase in the diffusion rate [17]. Recrystallization that takes place during the MSHT leads to grain coarsening. After AHT, a more homogenous distribution of the γ" was observed. This is expected since the precipitation of the γ" precipitates has a direct relationship with the Nb concentration in the matrix and the MSHT process leads to solutionizing the Nb that was segregated in the alloy before heat treatment [15]. Nb is highly susceptible to segregation and often happens in the solidification sequence of IN718 during cooling. It participates in the formation of precipitates such as NbC, δ-Ni_3Nb, and the Laves phases that can affect the mechanical properties of the part including tensile ductility, fatigue, and creep rupture properties [29].

Due to the sequential heating and cooling phenomena during the printing process, and induced stresses as a result of those, a high density of dislocations in the intergranular boundaries as well as in the matrix form. After the MSHT, the annihilation of the dislocations and the reduction in their densities as well as the dissolution of the secondary phases that formed during the printing process led to a drop in the hardness of the specimens. Also, the increase of the grain size and the release of the residual stresses from the manufacturing process might

contribute to the hardness reduction. These stresses are associated with the defects in the microstructure, including intergranular boundaries and dislocations that become mitigated by atomic diffusion at high temperatures [29]. The effect of the grain size on the mechanical properties has been comprehensively studied in literature and the well known Hall-Petch theory perfectly explains this relationship [52]. After aging, the strengthening precipitates, γ' and γ'', form and contribute to the hardness increase. The precipitation strengthening is primarily associated with the coherency strengthening that is attributed to the coherency strain between the matrix and the precipitate [53].

5. Conclusion

In the present study, the effectiveness of heat treatments consisting of a modified solutionization treatment and a two-stage aging treatment were evaluated for use in IN718 fabricated by LPBF. The primary findings are:

1. The rapid heating/cooling rate associated with LPBF led to columnar or cellular dendritic microstructure. Laves phases and carbides were formed along the cellular boundaries and interdendritic regions due to the segregation of Nb, Mo, and Ti in those areas. δ, γ'', and γ' precipitates were not observed in the as-built condition.
2. The solution heat treatment (1160 °C/4 h) entirely dissolved the Laves phases and produced a near-homogeneous microstructure with coarsened grains and carbides.
3. The heat treatment procedure discussed in this study resulted in a uniform distribution of γ'' and γ' precipitates which were slightly finer than those created with conventional heat treatments that were reported previously for AM-IN718.
4. Hardness values were observed to decrease following MSHT but increased substantially following the AHT process. Increased hardness is attributed to the precipitation of strengthening γ'' and γ' phases which were uniformly distributed within the γ matrix caused by the full dissolution of Laves phases and segregations after MSHT. It can be concluded that post-build heat treatments are able to enhance the microstructural and mechanical properties of LPBF-manufactured IN718.

Data availability statement

The raw/processed data required to reproduce these findings are available and can be shared upon request by contacting the corresponding author.

CRediT authorship contribution statement

Ali Tajyar: Writing – original draft, Formal analysis, Methodology, Writing – review & editing. **Nicholas Brooks:** Formal analysis, Writing – review & editing. **Noah Holtham:** Formal analysis, Writing – review & editing. **Russell Rowe:** Formal analysis. **David J. Newell:** Methodology. **Anthony N. Palazotto:** Methodology. **Keivan Davami:** Supervision, Funding acquisition, Formal analysis, Methodology, Writing – review & editing, All authors have read and agreed to the published version of the manuscript.

Declaration of competing interest

The authors declare that they have no known competing financial interests or personal relationships that could have appeared to influence the work reported in this paper.

Acknowledgement

The authors would like to thank the support of The U.S. Air Force Research Lab Summer Faculty Fellowship Program. Authors, Russell Rowe, Noah Holtham, and Keivan Davami extend gratitude to the Alabama Transportation Institute (ATI) for their support of the graduate student involved in this work. Keivan Davami acknowledges the support of the Advanced Manufacturing program of the National Science Foundation, award CMMI-AM #2029059.

Appendix A. Supplementary data

Supplementary data to this article can be found online at https://doi.org/10.1016/j.msea.2022.142770.

References

[1] The superalloys: fundamentals and applications - Roger C. Reed - Google Books, (n.d.). https://books.google.com/books?hl=en&lr=&id=SIUGcd4a-EkC&oi=fnd&pg=PA29&dq=The+Superalloys:+Fundamentals+and+Applications&ots=RpF-SEx1LQ&sig=_HQC2Y00d70mAKi-JDKxjZ6nLdg#v=onepage&q=The Superalloys%3A Fundamentals and Applications&f=false (accessed February 22, 2021).
[2] R. Jiang, A. Mostafaei, J. Pauza, C. Kantzos, A.D. Rollett, Varied heat treatments and properties of laser powder bed printed Inconel 718, Mater. Sci. Eng. 755 (2019) 170–180, https://doi.org/10.1016/j.msea.2019.03.103.
[3] R.B. Bhavsar, A. Collins, S. Silverman, Use of Alloy 718 and 725 in Oil and Gas Industry, (n.d).
[4] Additively Manufactured Inconel 718: Microstructures and Mechanical Properties - Dunyong Deng - Google Books, (n.d.).
[5] M.M. Attallah, R. Jennings, X. Wang, L.N. Carter, Additive manufacturing of Ni-based superalloys: the outstanding issues, MRS Bull. 41 (2016) 758–764, https://doi.org/10.1557/mrs.2016.211.
[6] E. Chlebus, K. Gruber, B. Kuźnicka, J. Kurzac, T. Kurzynowski, Effect of heat treatment on the microstructure and mechanical properties of Inconel 718 processed by selective laser melting, Mater. Sci. Eng. 639 (2015) 647–655, https://doi.org/10.1016/j.msea.2015.05.035.
[7] D. Deng, R.L. Peng, H. Brodin, J. Moverare, Microstructure and mechanical properties of Inconel 718 produced by selective laser melting: sample orientation dependence and effects of post heat treatments, Mater. Sci. Eng. 713 (2018) 294–306, https://doi.org/10.1016/j.msea.2017.12.043.
[8] J.R. Zhao, F.Y. Hung, T.S. Lui, Microstructure and tensile fracture behavior of three-stage heat treated inconel 718 alloy produced via laser powder bed fusion process, J. Mater. Res. Technol. 9 (2020) 3357–3367, https://doi.org/10.1016/j.jmrt.2020.01.030.
[9] D.J. Newell, R.P. O'Hara, G.R. Cobb, A.N. Palazotto, M.M. Kirka, L.W. Burggraf, J. A. Hess, Mitigation of scan strategy effects and material anisotropy through supersolvus annealing in LPBF IN718, Mater. Sci. Eng. 764 (2019), 138230, https://doi.org/10.1016/j.msea.2019.138230.
[10] M. Ni, C. Chen, X. Wang, P. Wang, R. Li, X. Zhang, K. Zhou, Anisotropic tensile behavior of in situ precipitation strengthened Inconel 718 fabricated by additive manufacturing, Mater. Sci. Eng. 701 (2017) 344–351, https://doi.org/10.1016/j.msea.2017.06.098.
[11] J. Str€, M. Terock, U. Glatzel, Mechanical and Microstructural Investigation of Nickel-Based Superalloy IN718 Manufactured by Selective Laser Melting (SLM) **, vol. 17, Wiley Online Libr, 2015, pp. 1099–1105, https://doi.org/10.1002/adem.201500158.
[12] R. Jiang, A. Mostafaei, Z. Wu, A. Choi, P.W. Guan, M. Chmielus, A.D. Rollett, Effect of heat treatment on microstructural evolution and hardness homogeneity in laser powder bed fusion of alloy 718, Addit. Manuf. 35 (2020), 101282, https://doi.org/10.1016/j.addma.2020.101282.
[13] D.T. Ardi, L. Guowei, N. Maharjan, B. Mutiargo, S.H. Leng, R. Srinivasan, Effects of post-processing route on fatigue performance of laser powder bed fusion Inconel 718, Addit. Manuf. 36 (2020), 101442, https://doi.org/10.1016/j.addma.2020.101442.
[14] D. Zhang, W. Niu, X. Cao, Z. Liu, Effect of standard heat treatment on the microstructure and mechanical properties of selective laser melting manufactured Inconel 718 superalloy, Mater. Sci. Eng. 644 (2015) 32–40, https://doi.org/10.1016/j.msea.2015.06.021.
[15] L. Zhou, A. Mehta, B. McWilliams, K. Cho, Y. Sohn, Microstructure, precipitates and mechanical properties of powder bed fused inconel 718 before and after heat treatment, J. Mater. Sci. Technol. 35 (2019) 1153–1164, https://doi.org/10.1016/j.jmst.2018.12.006.
[16] X. Li, J.J. Shi, G.H. Cao, A.M. Russell, Z.J. Zhou, C.P. Li, G.F. Chen, Improved plasticity of Inconel 718 superalloy fabricated by selective laser melting through a novel heat treatment process, Mater. Des. 180 (2019), 107915, https://doi.org/10.1016/j.matdes.2019.107915.
[17] T. Antonsson, H. Fredriksson, The effect of cooling rate on the solidification of INCONEL 718, 2005 361, Metall. Mater. Trans. B 36 (2005) 85–96, https://doi.org/10.1007/S11663-005-0009-0.
[18] A. Mostafa, I.P. Rubio, V. Brailovski, M. Jahazi, M. Medraj, Metals structure, texture and phases in 3D printed IN718 alloy subjected to homogenization and HIP treatments. https://doi.org/10.3390/met7060196, 2017.
[19] Y.-L. Kuo, T. Nagahari, K. Kakehi, materials The Effect of Post-Processes on the Microstructure and Creep Properties of Alloy718 Built Up by Selective Laser Melting, (n.d.). https://doi.org/10.3390/ma11060996.

[20] L.L. Parimi, G. Ravi, D. Clark, M.M. Attallah, Microstructural and texture development in direct laser fabricated IN718, Mater. Char. 89 (2014) 102–111, https://doi.org/10.1016/j.matchar.2013.12.012.
[21] D.H. Smith, J. Bicknell, L. Jorgensen, B.M. Patterson, N.L. Cordes, I. Tsukrov, M. Knezevic, Microstructure and mechanical behavior of direct metal laser sintered Inconel alloy 718, Mater. Char. 113 (2016) 1–9, https://doi.org/10.1016/j.matchar.2016.01.003.
[22] Y. Zhao, Q. Guo, Z. Ma, L. Yu, Comparative study on the microstructure evolution of selective laser melted and wrought IN718 superalloy during subsequent heat treatment process and its effect on mechanical properties, Mater. Sci. Eng. 791 (2020), 139735, https://doi.org/10.1016/j.msea.2020.139735.
[23] F. Yan, W. Xiong, E. Faierson, Grain structure control of additively manufactured metallic materials, Materials (Basel) 10 (2017) 1260, https://doi.org/10.3390/ma10111260.
[24] T. DebRoy, H.L. Wei, J.S. Zuback, T. Mukherjee, J.W. Elmer, J.O. Milewski, A. M. Beese, A. Wilson-Heid, A. De, W. Zhang, Additive manufacturing of metallic components – process, structure and properties, Prog. Mater. Sci. 92 (2018) 112–224, https://doi.org/10.1016/j.pmatsci.2017.10.001.
[25] S. Holland, X. Wang, J. Chen, W. Cai, F. Yan, L. Li, Multiscale characterization of microstructures and mechanical properties of Inconel 718 fabricated by selective laser melting, J. Alloys Compd. 784 (2019) 182–194, https://doi.org/10.1016/j.jallcom.2018.12.380.
[26] E. Brandl, U. Heckenberger, V. Holzinger, D. B, Additive Manufactured AlSi10Mg Samples Using Selective Laser Melting (SLM): Microstructure, High Cycle Fatigue, and Fracture Behavior, M.& Design, Undefined, Elsevier, 2012 (n.d.).
[27] S. Leuders, M. Thöne, A. Riemer, T. Niendorf, T. Tröster, H.A. Richard, H.J. Maier, On the mechanical behaviour of titanium alloy TiAl6V4 manufactured by selective laser melting: fatigue resistance and crack growth performance, Int. J. Fatig. 48 (2013) 300–307, https://doi.org/10.1016/j.ijfatigue.2012.11.011.
[28] A.N. Jinoop, C.P. Paul, S.K. Mishra, K.S. Bindra, Laser Additive Manufacturing using directed energy deposition of Inconel-718 wall structures with tailored characteristics, Vacuum 166 (2019) 270–278, https://doi.org/10.1016/j.vacuum.2019.05.027.
[29] W.M. Tucho, P. Cuvillier, A. Sjolyst-Kverneland, V. Hansen, Microstructure and hardness studies of Inconel 718 manufactured by selective laser melting before and after solution heat treatment, Mater. Sci. Eng. 689 (2017) 220–232, https://doi.org/10.1016/j.msea.2017.02.062.
[30] D. Liu, W.A. Miller, K.T. Aust, Diffusion induced grain boundary migration in Ni-Cu Diffusion couples, Acta Metall. 37 (1989) 3367–3378, https://doi.org/10.1016/0001-6160(89)90209-5.
[31] V.R. Chary, S.P. Gupta, Diffusion induced grain boundary migration in the Ag-Zn system, Mater. Char. 60 (2009) 1202–1213, https://doi.org/10.1016/j.matchar.2008.08.014.
[32] Refractory Carbides - Google Books, (n.d.).
[33] G.A. Knorovsky, M.J. Cieslak, T.J. Headley, A.D. Romig, W.F. Hammetter, Inconel 718: a solidification diagram, Metall. Trans. A 20 (1989) 2149–2158, https://doi.org/10.1007/BF02650300.
[34] J.E. Matz, T.W. Eagar, Carbide Formation in Alloy 718 during Electron-Beam Solid Freeform Fabrication, (n.d).
[35] X. Li, J.J. Shi, C.H. Wang, G.H. Cao, A.M. Russell, Z.J. Zhou, C.P. Li, G.F. Chen, Effect of heat treatment on microstructure evolution of Inconel 718 alloy fabricated by selective laser melting, J. Alloys Compd. 764 (2018) 639–649, https://doi.org/10.1016/j.jallcom.2018.06.112.
[36] K.N. Amato, S.M. Gaytan, L.E. Murr, E. Martinez, P.W. Shindo, J. Hernandez, S. Collins, F. Medina, Microstructures and mechanical behavior of Inconel 718 fabricated by selective laser melting, Acta Mater. 60 (2012) 2229–2239, https://doi.org/10.1016/j.actamat.2011.12.032.
[37] D. Paulonis, J. Oblak, D. Duvall, Precipitation in Nickel-Base Alloy 718, 1969.
[38] A. Devaux, L. Nazé, R. Molins, A. Pineau, A. Organista, J.Y. Guédou, J.F. Uginet, P. Héritier, Gamma double prime precipitation kinetic in Alloy 718, Mater. Sci. Eng. 486 (2008) 117–122, https://doi.org/10.1016/j.msea.2007.08.046.
[39] H. Zhang, D. Gu, C. Ma, M. Guo, J. Yang, R. Wang, Effect of post heat treatment on microstructure and mechanical properties of Ni-based composites by selective laser melting, Mater. Sci. Eng. 765 (2019), 138294, https://doi.org/10.1016/j.msea.2019.138294.
[40] X. Yu, X. Lin, F. Liu, L. Wang, Y. Tang, J. Li, S. Zhang, W. Huang, Influence of post-heat-treatment on the microstructure and fracture toughness properties of Inconel 718 fabricated with laser directed energy deposition additive manufacturing, Mater. Sci. Eng. 798 (2020), 140092, https://doi.org/10.1016/j.msea.2020.140092.
[41] F. Liu, X. Lin, G. Yang, M. Song, J. Chen, W. Huang, Recrystallization and its influence on microstructures and mechanical properties of laser solid formed nickel base superalloy Inconel 718, Rare Met. 30 (2011) 433–438, https://doi.org/10.1007/s12598-011-0319-0.
[42] Z. Wang, K. Guan, M. Gao, X. Li, X. Chen, X. Zeng, The microstructure and mechanical properties of deposited-IN718 by selective laser melting, J. Alloys Compd. 513 (2012) 518–523, https://doi.org/10.1016/j.jallcom.2011.10.107.
[43] W. Le, Z. Chen, K. Yan, S. Naseem, Y. Zhao, H. Zhang, Z. Zhang, Early evolution of δ phase and coarse γ'' phase in Inconel 718 alloy with high temperature ageing, Mater. Char. 180 (2021), 111403, https://doi.org/10.1016/J.MATCHAR.2021.111403.
[44] X. You, Y. Tan, S. Shi, J.M. Yang, Y. Wang, J. Li, Q. You, Effect of solution heat treatment on the precipitation behavior and strengthening mechanisms of electron beam smelted Inconel 718 superalloy, Mater. Sci. Eng. 689 (2017) 257–268, https://doi.org/10.1016/J.MSEA.2017.01.093.
[45] S.H. Zhang, H.Y. Zhang, M. Cheng, Tensile deformation and fracture characteristics of delta-processed Inconel 718 alloy at elevated temperature, Mater. Sci. Eng. 528 (2011) 6253–6258, https://doi.org/10.1016/J.MSEA.2011.04.074.
[46] S. Azadian, L.Y. Wei, R. Warren, Delta phase precipitation in Inconel 718, Mater. Char. 53 (2004) 7–16, https://doi.org/10.1016/J.MATCHAR.2004.07.004.
[47] S. Gribbin, S. Ghorbanpour, N.C. Ferreri, J. Bicknell, I. Tsukrov, M. Knezevic, Role of grain structure, grain boundaries, crystallographic texture, precipitates, and porosity on fatigue behavior of Inconel 718 at room and elevated temperatures, Mater. Char. 149 (2019) 184–197, https://doi.org/10.1016/J.MATCHAR.2019.01.028.
[48] M. Sundararaman, P. Mukhopadhyay, S. Banerjee, Precipitation of the δ-Ni3Nb phase in two nickel base superalloys, 1988 193, Metall. Trans. A 19 (1988) 453–465, https://doi.org/10.1007/BF02649259.
[49] M.R. Ahmadi, E. Povoden-Karadeniz, K.I. Öksüz, A. Falahati, E. Kozeschnik, A model for precipitation strengthening in multi-particle systems, Comput. Mater. Sci. 91 (2014) 173–186, https://doi.org/10.1016/j.commatsci.2014.04.025.
[50] Kou: welding metallurgy - Google scholar, (n.d.). https://scholar.google.com/scholar_lookup?title=Welding.Metallurgy&publication_year=2003&author=S.Kou (accessed December 18, 2021).
[51] S.A. David, J.M. Vitek, Correlation between solidification parameters and weld microstructures, Https://Doi.Org/10.1179/Imr.1989.34.1.213. 34 (2013) 213–245. https://doi.org/10.1179/IMR.1989.34.1.213.
[52] Y.C. Yeoh, G. Macchi, E. Jain, B. Gaskey, S. Raman, G. Tay, D. Verdi, A. Patran, A. M. Grande, M. Seita, Multiscale microstructural heterogeneity and mechanical property scatter in Inconel 718 produced by directed energy deposition, J. Alloys Compd. 887 (2021), 161426, https://doi.org/10.1016/J.JALLCOM.2021.161426.
[53] S. Zhang, X. Lin, L. Wang, X. Yu, Y. Hu, H. Yang, L. Lei, W. Huang, Strengthening mechanisms in selective laser-melted Inconel718 superalloy, Mater. Sci. Eng. 812 (2021), 141145, https://doi.org/10.1016/J.MSEA.2021.141145.